Bifunctional OER and ORR Electrocatalyst based on cobalt oxide nanocrystals: Towards Rechargeable Metal-air Batteries.

A thesis submitted towards partial fulfillment of
BS-MS Dual Degree Programme

By

Mohammed Fawaz P A
(BS-MS student, Registration No.: 20121059)

Under the guidance of,

Dr. P. A. Joy,
Chair, Physical& Materials chemistry division,
National Chemical Laboratory, NCL
Pune, India

Certificate

This is to certify that this dissertation entitled **"Bifunctional OER and ORR Electrocatalyst based on cobalt oxide nanocrystals: Towards Rechargeable Metal-air Batteries."** towards the partial fulfillment of the BS-MS dual degree programme at the Indian Institute of Science Education and Research Pune, represents original research carried out by **Mohammed Fawaz P A** at National Chemical Laboratory, Pune Under the supervision of **"Dr. P. A. Joy, Chair, Physical& Materials chemistry division, National Chemical Laboratory, Pune"** during the academic year of 2016-2017.

Date:

Place: Pune

Dr. P. A. Joy

Chair, Physical & Materials chemistry Division

NCL Pune

Declaration

I hereby declare that the matter embodied in the report entitled **"Bifunctional OER and ORR Electrocatalyst based on cobalt oxide nanocrystals: Towards Rechargeable Metal-air Batteries."**are the results of the investigations carried out by me at National Chemical Laboratory Pune and the Department of Chemistry , IISER Pune, Under the supervision of **"Dr. P. A. Joy, Chair, Physical& Materials chemistry division, National Chemical Laboratory, Pune"**and the same has not been submitted elsewhere for any other degree.

Mohammed Fawaz P. A

Date: 23/10/2017

Place: Pune

Acknowledgement

To my mentors **Dr. P. A. Joy, Chair, Physical & Materials chemistry division, National Chemical Laboratory, Pune** and **Dr. Muhammed Musthafa O.T., Assistant Professor, Department of Chemistry IISER Pune :**because I owe it all to you. Many thanks!

I am grateful to **Dr.Ramsundar** for providing basic knowledge in synthesis. I am also grateful to **Dr.Ravikumar** for his valuable advises.

A very special gratitude goes out to **Neethu C D**. She was very keen to know every step of my research life and was a moral and emotional support throughout.

With a special mention to **Zahid Manzoor Bhat, Alagar Raja, Mruthyunjayachari, Manu Gautam, Mohan, Manjunath, Anupriya** and all other Lab mates. It was a great experience working alongside all you folks. I will miss our tea sessions.

I sincerely thank **Dr. Pramod Pillai** for giving consent to use UV-Vis and **Soumendu Roy** for helping with the same. I also thank **Ajith V J** for the assistance with Raman instrument. I am also grateful to National Chemical Laboratory: Thank you for the workspace and assistance.

To my all friends, Especially **Favaz Ahammed, Prasanth P, Akhil N B, Aswin Pradeep and Thasneem Aliyar** who supported me all the way of my IISER life, thanks for making this a happy ride.

List of tables

List of illustrations

TABLE OF CONTENTS

ABSTRACT

Catalyst for oxygen evolution reaction (OER) and oxygen reduction reaction (ORR) are at the heart of key renewable energy technologies such as water splitting and rechargeable batteries. But developing low cost oxygen electrode catalyst with high activity at low over potential remains a great challenge. Owing to the high cost of Ruthenium and Iridium metal based oxides and its limited availability, research on alternative catalyst based on non-noble metals and their oxides have been pursued worldwide. Spinel-type cobalt oxide, Co_3O_4, with multiple oxidation states of cobalt, is an alternate choice for OER and ORR activities. The objective of the present work is to exploit the scope of cobalt oxide and to selectively tune its electrocatalytic activity by substitution by other transition metal ions to make a better electrocatalyst with higher activity and improved stability. Here we synthesized Manganese cobalt spinel oxide nanocrystals with different manganese content by autocombustion method and studied the effect on the electrocatalytic Oxygen reduction and oxygen evolution reaction to make use this as a bifunctional catalyst in electrochemical energy devices such as rechargeable Metal - Air batteries

Chapter 1. INTRODUCTION

Energy plays a crucial role in everyday life. The demand for developing sustainable and clean energy become important in this era[1, 2]. We have to focus on renewable energy resources[3, 4] and sustainable energy storage devices which uses materials which are environment friendly, abundant as well as stable[5]. In the existing electrochemical energy storage and conversion devices such as fuel cell, batteries, supercapacitors, solar cells etc., metal air batteries have gained much attention due to its high energy density, flat discharge voltage, long shelf life[6], low cost and non-toxic (depending on the metal used).

Among the known metal-air batteries, using metals such as Li, Na, Mg, K, Ca, Al, Ge, Fe and Zn, rechargeable Zn-air and Li-air batteries are the most studied in past decade[6,7]. Compared to Li-air battery, Zn-air battery components are stable towards moisture and air, which facilitate its assembly in ambient condition and not in an inert atmosphere as for the former. This gives an added advantage on manufacturing process of Zn-air batteries over Li-air batteries. Zn-air batteries is preferred due to the cost effectiveness, as expensive Li metal and the non-aqueous electrolytes are used in Li-air batteries compared to the cheaper Zn metal and the aqueous electrolytes. On considering the technical level for practical application Zn-air batteries are more favoured[7].

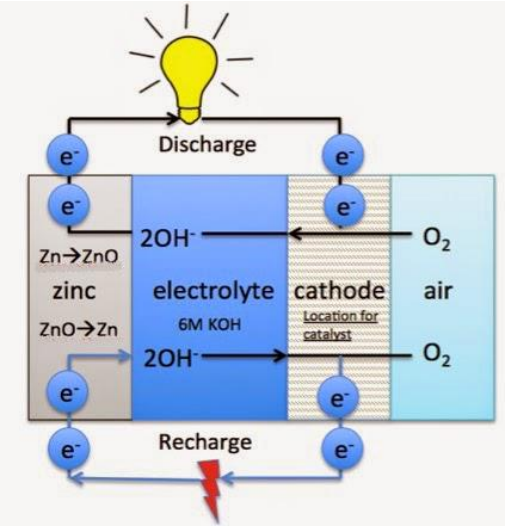

Figure 1.1: Schematic representation of rechargeable Zinc-air battery[8].

The two basic reaction that occur in rechargeable Zn-air battery are ORR (Oxygen reduction reaction) on discharge and OER (Oxygen Evolution Reaction) on charging. Electrocatalytic activity of the bifunctional catalyst towards these two elementary reaction will govern the efficiency of our battery[9].

1.1 Oxygen Reduction Reaction

Oxygen Reduction Reaction is the vital process in the Fuel cell and Metal - Air batteries in determining the working efficiency. ORR involves complex electrochemical reactions which includes multistep electron transfer and complicated oxygen containing species. Its mechanism is poorly understood because cleavage of oxygen bond involves four electrons and four protons[10]. It is generally recognized that ORR initiates with the adsorption of O_2 on the electrode surface and accepting an electrons and is reduced to H_2O or OH^-. ORR can happens via two different routes, two step 2 electron and one step 4 electron pathway.

In acid aqueous systems[10]

(1) The 4-electron reaction process

$$O_2 + 4H^+ + 4e^- \rightarrow 2H_2O \text{.....} E = 1.229\ V$$

(2) The 2-plus-2 electrons reaction process

$$O_2 + 2H^+ + 2e^- \rightarrow H_2O_2 \text{.....} E = 0.700\ V$$

$$2H_2O_2 + 2H^+ + 2e^- \rightarrow 2H_2O + O_2 \text{.....} E = 1.760\ V$$

In alkaline aqueous systems[10]

(1) The 4-electron reaction process

$$O_2 + 2H_2O + 4e^- \rightarrow 4OH^- \text{.....} E = 0.401\ V$$

(2) The 2-plus-2 reaction process

$$O_2 + H_2O + 2e^- \rightarrow HO^{2-} \text{.....} E = 0.065\ V$$

$$HO_2^- + H_2O + 2e^- \rightarrow 3OH^- \text{.....} E = 0.867\ V$$

Platinum shows higher activity towards ORR[11], but the higher costs limits its production. From the past decade, researchers are developing less expensive and

more abundant non-noble metal based catalyst such as transition metals Cu, Ti, metal oxides and metal alloys have been studied[12-14].

1.2 Oxygen evolution reaction

OER is a key step involved in water splitting devices and metal-air batteries. OER consist of four-electron oxidation of two water molecules and removal of four protons to form oxygen-oxygen bond[10, 15].

In acid aqueous electrolyte[10]

$$2H_2O \rightarrow O_2 \uparrow + 4H^+ + 4e^- \ldots\ldots\ldots\ldots\ldots\ldots\ldots E= 1.229\ V$$

In alkaline electrolyte[9]

$$4OH^- \rightarrow O_2 \uparrow + 2H_2O + 4e^- \ldots\ldots\ldots\ldots\ldots\ldots E= 0.401\ V$$

This reactions need high overpotential and kinetically not favorable. For a better OER catalyst it should be able to give a higher current density at lower overpotential and of course stability, low cost and abundance[16]. Oxides of noble metals Iridium & ruthenium is well known OER catalyst but its higher cost and less availability makes people to think about an alternative[17-19]. So that there are several catalyst has been found. First row transition metal oxides such as MnO_2, Co_3O_4 and Graphene hybrids of cobalt oxide are found to be having higher OER activity[20-22].

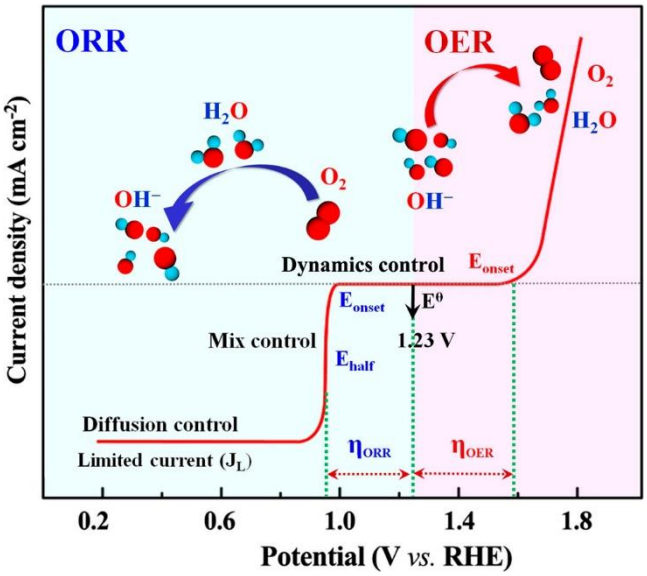

Figure 1.2: Oxygen Reduction Reaction (ORR) and Oxygen Evolution Reaction (OER) polarization curve [10]

Spinels formed by transition metal oxides are well known to show catalytic activity towards ORR/OER in alkaline and non-aqueous media. Their activity, availability, low cost, easy synthesis, thermodynamic stability, environmental friendliness make them more suitable for an electrocatalysis[10, 23]. The presence of both tetrahedral and octahedral sites simultaneously provides multiple sites to accommodate different transition metal cations. Co_3O_4 is well known from 1980s in which presence of Co^{2+} and Co^{3+} in the tetrahedral and octahedral site is the main cause for its promising activity towards electrocatalytic ORR and OER[24]. To increase the activity further people are used different methodologies like Co_3O_4/GO hybrid and Co_3O_4-Nitrogen doped rGO[25].

In this present study we are trying to selectively tune the elecrocatalytic activity of cobalt oxide by making substitution with transition metal manganese and investigating the activity and understanding the role of various oxidation states present in the metal cations towards the electrocatalytic activity, and to use as a bifunctional catalyst in rechargeable Metal–Air batteries. Nanocrystals of cobalt oxide and its mixed metal composites $Mn_xCo_{3-x}O_4$ have been successfully synthesized by an autocombustion method and characterized by a range of techniques such as X-ray diffraction (XRD), Field emission scanning microscopy (FESEM), Fourier transform Infrared spectroscopy (FTIR) and Raman spectroscopy. Activity towards ORR and OER are extracted from different electrochemical techniques.

Chapter 2. MATERIALS & METHOD

2.1 CHEMICALS USED

Cobalt Nitrate $Co(NO_3)_2.6H_2O$ (Sigma-Aldrich), Manganese Nitrate $Mn(NO_3)_2.6H_2O$ (Sigma-Aldrich), Glycine H_2NCH_2COOH (MERCK), Carbon powder (Vulcan Carbon), Isopropyl alcohol (IPA) (C_3H_8O), Polytetrafluoroethylene (PTFE), Sodium Hydroxide (NaOH)

2.2 SYNTHESIS PROCEDURE

Co_3O_4 nanocrystals were synthesized by a one-step solution-combustion or auto combustion method, by using glycine (H_2NCH_2COOH) as a fuel. Stoichiometric amount of metal nitrates were dissolved in minimum amount of distilled water. Glycine was dissolved in water and mixed with the metal nitrate solution. The mixed solution was sonicated for 15 minutes and transferred to preheated dish at about 200 ^oC. After complete evaporation of water, the resulting viscous liquid get ignited by itself giving rise to fine powder of metal oxides.

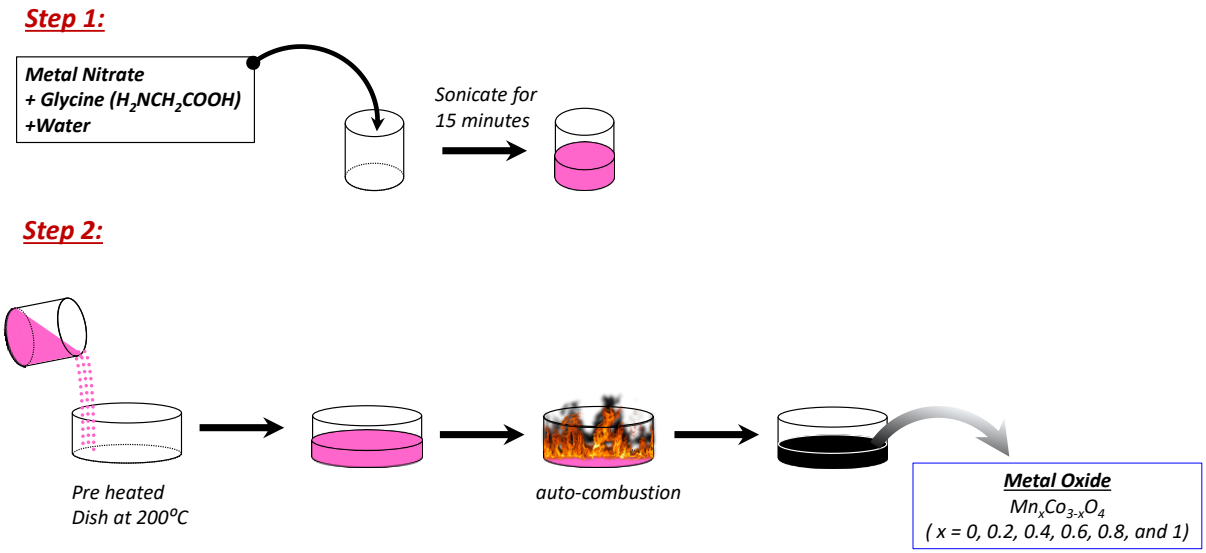

Figure 2.2.1: Schematic representation of synthesis procedure

Glycine which is the simplest amino acid assists two basic purposes. First, being oxidized by the nitrate ions as a fuel for this reaction, second, it will form complex with the metal cation, which in turn increase the solubility and avoid the selective

precipitation when water is evaporated. Both carboxylic and amine group can involve in complexation with metal cations. This 'zwitter' ionic nature helps them to make complexation with metal cations of different ionic size. Transition metals do make complexation with the amine group[26].

Metal to Glycine ratio was optimized to get pure, homogeneous and minimum particle sized nanocrystals. Same optimized glycine ratio was used to synthesize nanocrystals of $Mn_xCo_{3-x}O_4$ were x = 0.2, 0.4, 0.6, 0.8, and 1 and these are labeled as MCo-2, MCo-4, MCo-6, MCo-8 and MCo-10, respectively.

2.3 EXPERIMENTAL SECTION

2.3.1 Cyclic voltammetry (CV)

Mixture of 4 mg of catalyst, 1 mg of Vulcan carbon and 5% wt of PTFE solution were dispersed in isopropanol solvent and sonicated for 30 minutes to form homogenous ink. Then 5 µl of this catalyst ink was loaded onto glassy carbon electrode of 3 mm diameter. Cyclic voltammetry (using VMP-300 instrument) was conducted in an electrochemical cell using Mercury-Mercury oxide (Hg/HgO) electrode, platinum mesh and catalyst drop casted glassy carbon, as reference, counter and working electrode respectively. Electrolyte 1 M NaOH was saturated with nitrogen by purging nitrogen gas prior to the start of the experiment. The working electrode was cycled before the data were recorded at a scan rate of 20 mV/s.

2.3.2 Rotating Disk Electrode (RDE)

For measurements, catalysts were prepared same as cyclic voltammetry. 5 µl ink was loaded on a glassy carbon rotating disk electrode of 5 mm diameter (PAR STAT instrument). The working electrode were scanned in both ORR and OER region at 1 mV/s, 1600 RPM in oxygen saturated electrolyte. With different RPM (400,900,1600,2500,3600) and from the resulted Koutecky – Levich (K-L) plot (I^{-1} vs $\omega^{-1/2}$) best linear fit were used to calculate the number of electrons transferred (n) in the ORR pathway.

2.3.3 Rotating Ring Disk Electrode (RRDE)

With the same catalyst ink, glassy carbon disk and pt ring electrode (GC-Pt) as working electrode. Faradaic efficiency was measured from the ring current collected.

The disk electrode was held at a constant 10mA/cm^2 current density per geometric area[16].

$$\varepsilon = \frac{2i_r}{i_d N}$$

i_r = Ring current

i_d= Disk current

N = collection efficiency

Collection efficiency was determined from reducing $K_3Fe(CN)_6$ at the GC-Pt ring electrode. Collection efficiency is given by i_r/i_d.

2.3.4 Electrochemical Active Surface Area (ECSA)

Electrochemical surface area of each catalyst is determined by measuring electrochemical double layer capacitance of the catalyst surface. The non-faradaic region has scanned at different scan rates and the corresponding current has been noted. The double layer charging current (i_c), is equal to the product of the scan rate, υ, and the double layer capacitance(C_D) [16].

$$i_c = \upsilon C_D$$

The plot of double layer current as a function of scan rate results in a linear plot with a slope equal to the double layer capacitance of the electrode. ECSA is given by

$$\text{ECSA} = \frac{C_D}{C_S}$$

Where Cs is the specific capacitance or the capacitance of the smooth planar surface.

2.3.5 RHE Calibration

All the measurements were done using standard calomel electrode as reference electrode. It was calibrated with respect to RHE. Electrolyte was saturated with hydrogen gas with Pt as working electrode and performed cyclic voltammetry at 10mV/s scan rate. Average of the two potentials at which the current crossed zero was taken to be the thermodynamic potential for the hydrogen electrode reactions.

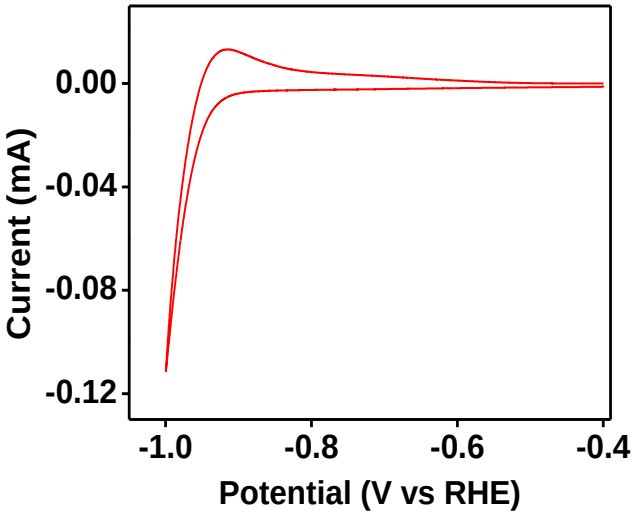

Figure 2.3.1: Hydrogen evolution reaction (HER) on Pt WE in 1M NaOH, E_{RHE} = E (Hg/HgO) + 0.91V

Electrodes used:

Working electrodes: Glassy carbon (0.076, 0.031 cm^2), Platinum mesh electrode, Glassy carbon disc-Platinum ring electrode.

Reference electrode: Mercury-Mercury oxide (Hg/HgO) (E_{RHE}= +0.910 V, 1 M NaOH)

Counter electrode: Platinum mesh electrode

Table 2.1: Instruments used

Sl no	Instrument	Technique
1	PANalytical X'Pert	XRD
2	ATR-FTIR (Bruker Alpha FTIR Spectrometer System)	IR spectroscopy
3	LAB-RAM HR 800	Raman spectroscopy
4	UV-3600 Plus UV-VIS-NIR spectrophotometer	UV-Vis spectroscopy
5	VMP-300 Electrochemical Work Station (Biologics)	Electro chemicals analysis
6	PARSTAT MC (Ametek)	RDE, RRDE

2.4 TECHNIQUES

2.4.1 X-ray diffraction

X-rays, which is a part of electromagnetic spectrum with a wavelength 0.5 - 2.5 A°, which is the same order of magnitude as the typical inter-atomic/inter-planar distances in polycrystalline solids. Therefore it is commonly used for the determination of crystal structure, grain size, lattice parameter, strains, defects etc.

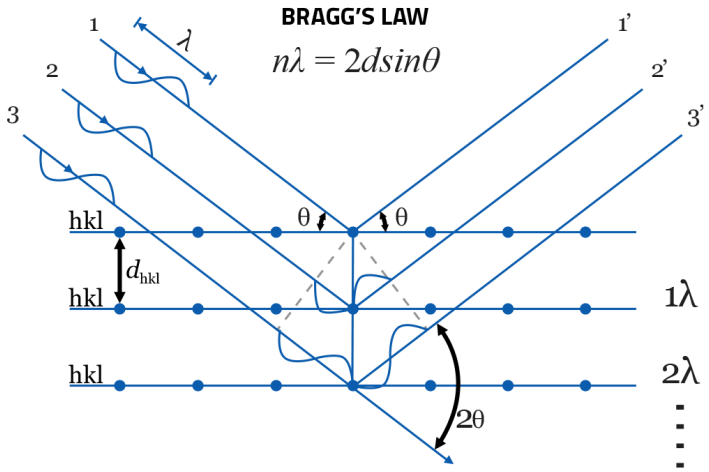

Figure 2.4.1: Schematic representation of X-ray diffraction from crystal planes[27]

As X-Rays falls on the sample it interact with electron cloud of regularly arranged atoms in a crystal and cause diffraction to the beam. These diffracted beam undergo constructive as well as destructive interference. These constructively interfered beams are detected. By using the Braggs law

$$n\boldsymbol{\lambda} = 2\boldsymbol{d}\ \boldsymbol{sin}\ \boldsymbol{\theta}$$

λ- Wavelength of the incident X-rays — n- order of diffraction

d- interplanar spacing of the crystal — **θ**- the angle of incidence

Which relates the wavelength of electromagnetic radiation to the diffraction angle and the lattice spacing in a crystalline sample. By scanning the sample through a range of 2θ angles, facilitates to obtain all possible diffraction directions of the lattice due to the random orientation of the powdered material[28].

2.4.2 Attenuated Total Reflectance (ATR) FT-IR Spectroscopy

IR spectroscopy uses wavelength ranging from 500 cm^{-1} to 4000 cm^{-1}. As vibration frequency of them falls in this range, it helps to identify the functional groups in the molecule.

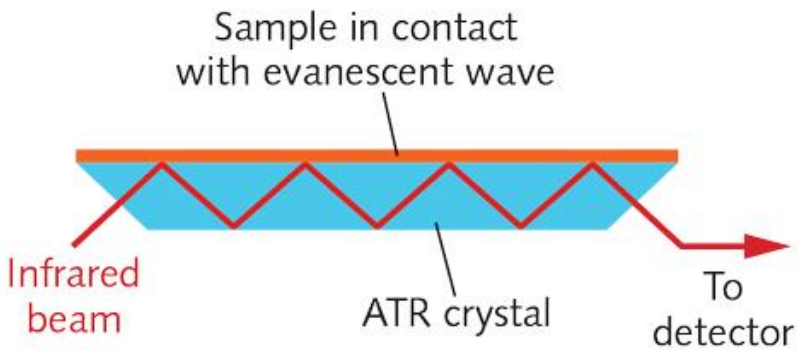

Figure 2.4.2: Schematic representation of Attenuated Total Reflectance (ATR) IR Spectroscopy[29]

ATR-IR works based on the principle of total internal reflection. Optically dense crystal such as Diamond, Zinc Selenide (ZnSe), Germanium with a high refractive index is being used to facilitate total internal reflection as infrared beam hit on this at a particular angle. An evanescent wave is produce due to this internal reflection. This wave extends beyond the surface of the crystal into the sample held in contact with the crystal. Evanescent wave would be attenuated as sample absorbs energy and thus some region of IR beam. The IR beam which comes out through the opposite end is send to the detector which gives us infrared spectrum. As the evanescent wave extends to about 0.5-5 μm from crystal surface, sample should be in close contact with crystal[30].

2.4.3 Raman spectroscopy

Similar to IR, Raman uses the same wavelength range for detection and both gives information about vibrational frequency. Raman spectra probes vibrational modes with changes in polarizability while IR spectra focus on net dipole moment. Therefore information obtained is entirely different.

Raman spectra is an emission of electromagnetic waves shifted in energy from the incident radiation. Source used in Raman is highly coherent laser source. Laser is focused on the sample, Raman scattered rays reach the detector. Compared to

antistokes, stokes shows more intensity, therefore generally stokes is being used for analysis.

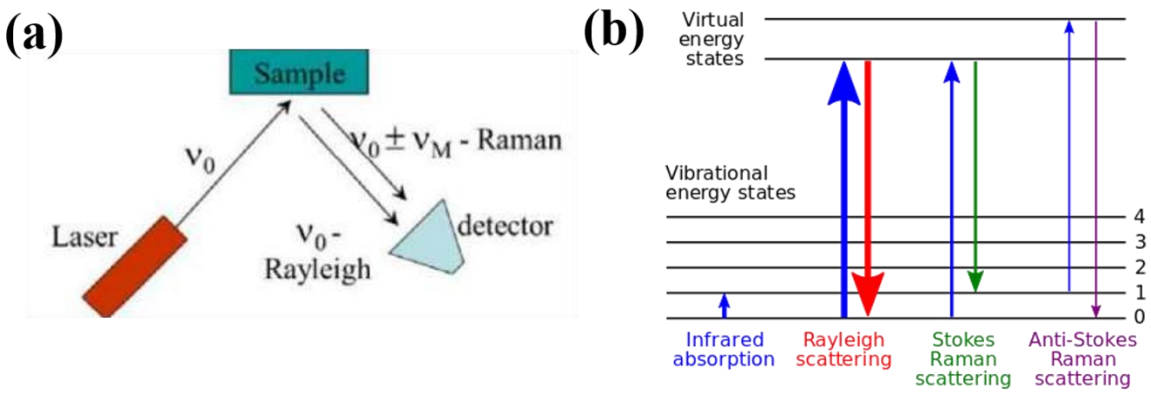

Figure 2.4.3: (a) Basic principles of Raman analyser. (b) Possible scattering radiations[31, 32]

2.4.4 UV-Vis spectroscopy

The amount of light absorbed or transmitted or reflected by the sample with respect to the incident beam is monitored in UV-Vis spectroscopy. It gives information about electronic transitions as it uses wavelength ranging from 190nm to 900nm.

Beer-Lambert-Bouguer law, generally called the Beer-Lambert law suggests that the absorbance (A) is directly proportional to[33]

$$A \; \alpha \; Cl$$

$$A = -log_{10} \left\{\frac{I_T}{I_0}\right\} = -\boldsymbol{\epsilon}\, Cl$$

C - Concentration of the sample L - path length

I_0- intensity on input light I_T- intensity of transmitted light

$\boldsymbol{\epsilon}$ - molar absorption coefficient

2.4.5 Electrochemical techniques

2.4.5.1 Cyclic voltammetry (CV)

Cyclic voltammetry is an electrochemical technique, where current is measured while applying a varying potential on the working electrode. Generally done in three electrode system, working electrode (WE) where the electrochemical reaction of

analyte in the solution in which it is immersed occur, Counter electrode (CE) helps to complete the circuit, Reference electrode (RE) which helps to sense the potential variation at WE. Current is measured across WE and CE. Potential is measured across WE and RE. This technique is used to study electrochemical character of analyte in the solution.

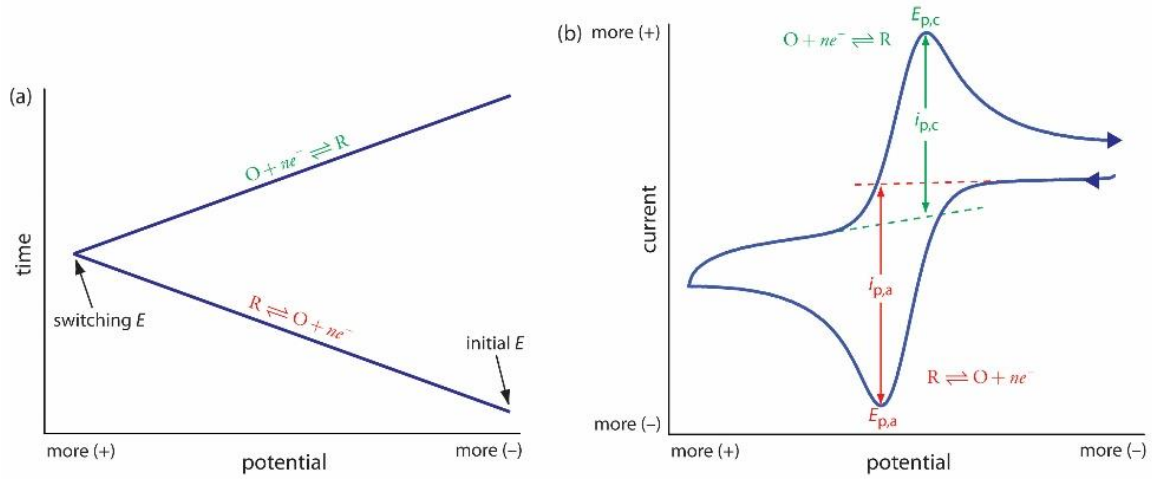

Figure 2.4.4: (a) The applied voltage on working electrode with respect to time and (b) the current response of this applied voltage[34].

For reversible system: 1) $\frac{i_{pa}}{i_{pc}}$ = 1

2) $E_{pa} - E_{pc} = \frac{0.059}{n}$ (n= no of electron)

For non-reversible or quasi reversible: 1) $\frac{i_{pa}}{i_{pc}} \neq 1$

2.4.5.1.1 Randles sevcik equation: It describes the effect of scan rate on the peak current *I*[35].

$$I = 2.68 * 10^5 n^{2/3} A D^{1/2} C \upsilon^{1/2}$$

i - peak current (A)
n - number of electrons
A - electrode area (cm^2)
F - Faraday Constant (96485 C mol^{-1})
D - diffusion coefficient ($cm^2\ s^{-1}$)
C - concentration (mol cm^{-3})
v - scan rate (V s^{-1})
R - Gas constant (J K^{-1} mol^{-1})
T - temperature (K)

I vs. $\upsilon^{1/2}$ plot gives a straight line with slope $2.68 * 10^5 n^{2/3} A D^{1/2} C$, from which unknown parameter can be deduced easily.

2.4.5.2 Rotating Disc Electrode (RDE) technique

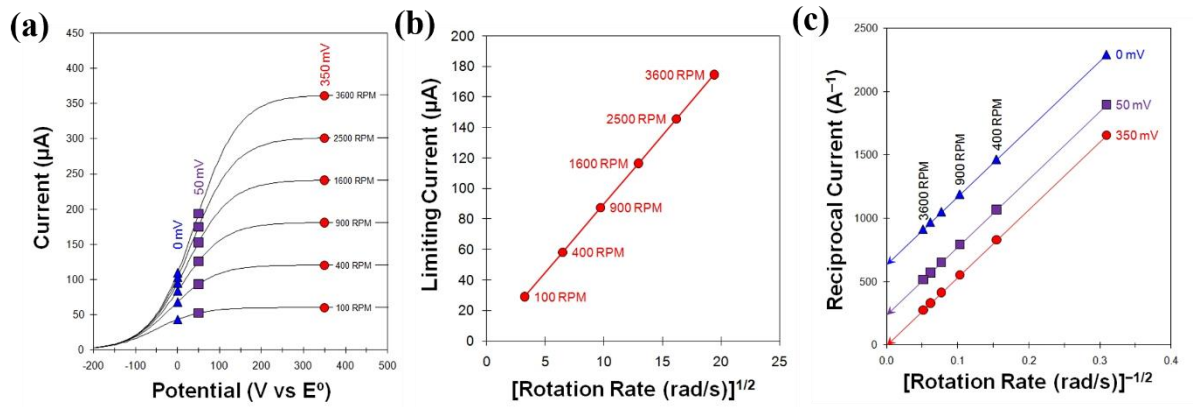

Figure 2.4.5: (a) RDE linear sweep voltammogram profile for oxidation, (b) Levich plot (c) Koutecky-levich plot[36].

Solution at quiescent stage gives CV profile as the one shown above. The decrease in current after peak potential is due to the diffusion limitation of analyte molecules. This diffusion limitation can be decreased via using this rotating electrode as working electrode (figure 2.4.5a) in three electrode system with CE, RE.As the electrode rotates hydrodynamic boundary layer is dragged and solution moves away from electrode center due to the centrifugal force. This cause upward perpendicular flow of analyte solution from bulk to replace the boundary layer. This cause the solution to flow towards and across the electrode. The flow rate can be controlled via the rotation rate of electrode. Levich plot and Koutecky-levich plot are used to elucidation of parameters from RDE technique[37].

2.4.5.2.1 Levich study: Levich plot with limiting current vs. square root of rotation rate, which gives a straight line with slope of $0.620nFAD^{2/3}v^{-1/6}C$ and intercept zero (figure 2.4.5 b).

$$i_L = 0.620nFAD^{2/3}v^{-1/6}C\ \omega^{1/2}$$

i_L- limiting current

n - no of electrons

F - Faradays constant (96485 C mol^{-1})

A - area of electrode (cm^2)

D - diffusion coefficient ($cm^2\ s^{-1}$)

υ - kinematic viscosity ($cm^2\ s^{-1}$)

C - concentration ($mol\ cm^{-3}$)

ω - rotation rate ($rad\ s^{-1}$)

2.4.5.2.2 Koutecky-levich study: In case of kinetic limitations at RDE-electrolyte interface, levich plot alone work as it won't be straight. The reciprocal of current (A) vs. reciprocal of square root of rotation rate (rad/sec), which gives a straight line with intercept of reciprocal of i_k (kinetic current) and slope reciprocal of $0.620nFAD^{2/3}\upsilon^{-1/6}C$ according to the equation below is called Koutecky-levich plot (figure 2.3c).

$$\frac{1}{i} = \frac{1}{i_k} + \frac{1}{i_L}$$

$$\frac{1}{i} = \frac{1}{i_k} + \frac{\omega^{-1/2}}{(0.620nFAD^{2/3}\upsilon^{-1/6}C)}$$

i_L - Limiting current

n - no of electrons

F - faradays constant (96485 C mol^{-1})

A - area of electrode (cm^2)

D - diffusion coefficient (cm^2 s^{-1})

υ - kinematic viscosity (cm^2 s^{-1})

C - concentration (mol cm^{-3})

ω - rotation rate (rad s^{-1})

With this i_k kinetic current we can estimate rate constant of the reaction.

2.4.5.3 Rotating Ring Disc Electrode (RRDE) technique

RRDE is also done in three electrode setup, CE, RE and rotatable WE which have disc in the middle surrounded by a ring. The disc and ring act as two different working electrodes. So the reaction on it can be controlled and monitored with respect to potential we apply[38]. As the product from disc radially move out wards this can be sensed with the ring. RRDE is used to show the reversibility, to find out presence of different type of complex reactions and mechanistic elucidation by detecting transient and short lived reaction intermediates.

Chapter 3. RESULTS & DISCUSSION

3.1 PHYSICO CHEMICAL CHARACTERIZATION

All the six compounds were characterized by different techniques. Crystal structure, phase composition and crystallite size were studied by X-ray diffraction (XRD), elemental compositions were investigated from SEM/EDS studies and further samples were subjected to Fourier transform Infrared spectroscopy (FTIR) and Raman spectroscopy to understand the bond nature and substitution sites.

It is observed that Co_3O_4 nanocrystals and different substituted compositions are formed in single phase and homogeneous form as evidenced from XRD patterns (Figure 3.1). The cubic lattice parameter (a) was obtained from the XRD patterns by using the Powder cell software. The average crystallite size was calculated using the Scherrer formula, $D=K\lambda/\beta\cos\Theta$, where D is the crystallite size, λ= 0.15418 nm, K=0.89, β= (FWHM/180°)*3.14, and Θ is the diffraction angle, FWHM is the diffraction peak width at half-maximum height, respectively[39].

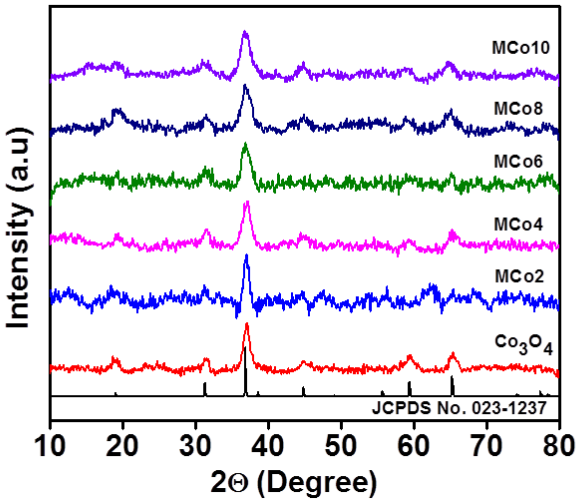

Figure 3.1: XRD patterns of synthesized compounds.

It is found that the lattice parameter (Table 3.1) is increasing gradually with increase in the manganese in the composition. This is due to the larger ionic size of manganese which is having higher ionic radius (r^{3+}_{Mn} = 0.645 Å) than that of cobalt (r^{3+}_{Co} = 0.545 Å) so that the lattice is expanded to accommodate the larger ions.

Crystallite size is found to be between 6-9 nm calculated using the Scherrer formula (Table 3.1).

Table 3.1: Lattice parameter and crystallite size of the synthesized nanocrystals.

Sample	*Lattice parameter (Å)*	*Crystallite size (nm)*
Co3O4	8.086	9
MCo-2	8.094	8
MCo-4	8.116	7
MCo-6	8.120	6
MCo-8	8.137	6
MCo-10	8.173	6

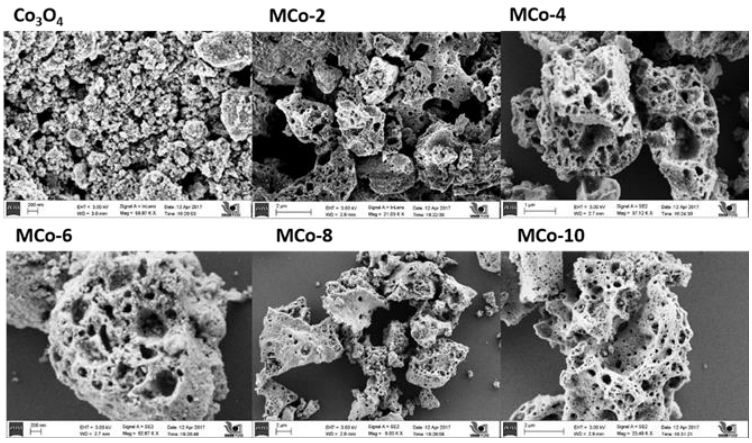

Figure 3.2: FESEM images of synthesized $Mn_xCo_{3-x}O_4$ composite nanocrystals.

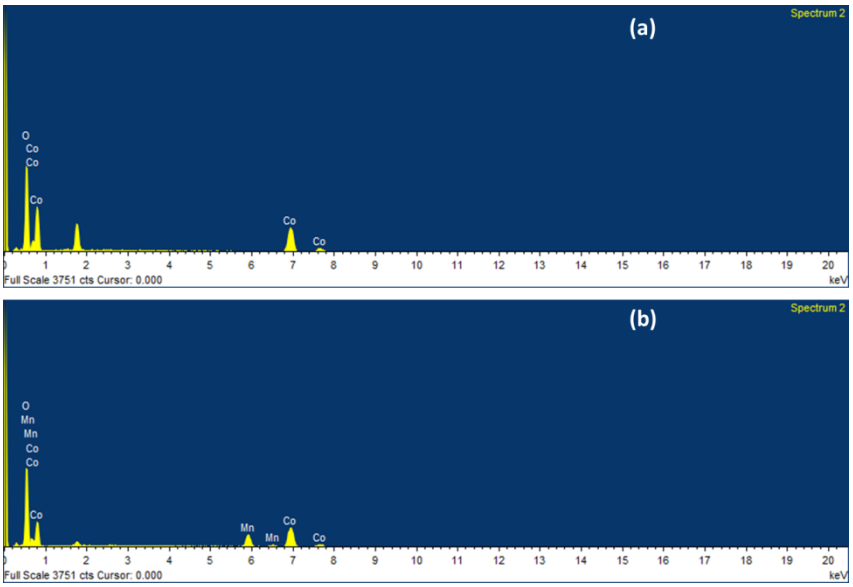

Figure 3.3: EDS patterns (a) Co_3O_4 and (b) MCo-10

FESEM images (Figure 3.2) show that the materials are having porous nature because of the gases are coming out after the reaction and from EDS patterns (Figure 3.3) it is clear that manganese incorporation into the Co_3O_4 spinel.

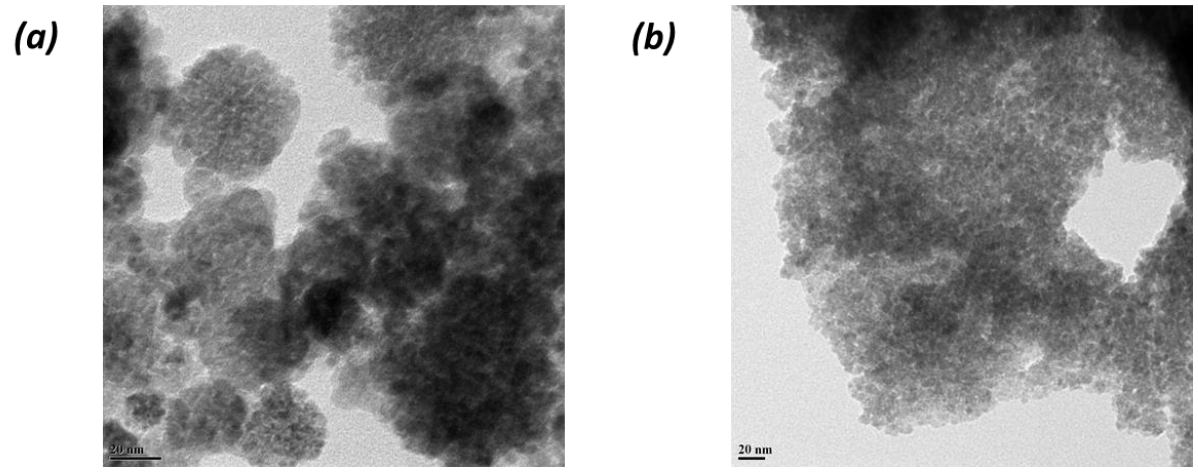

Figure 3.4: TEM images of (a) Co_3O_4 and (b) MCo-4.

TEM images (Figure 3.4) shown that nanocrystals are spherical particles and agglomerated. Size of the crystals are matching with the XRD studies.

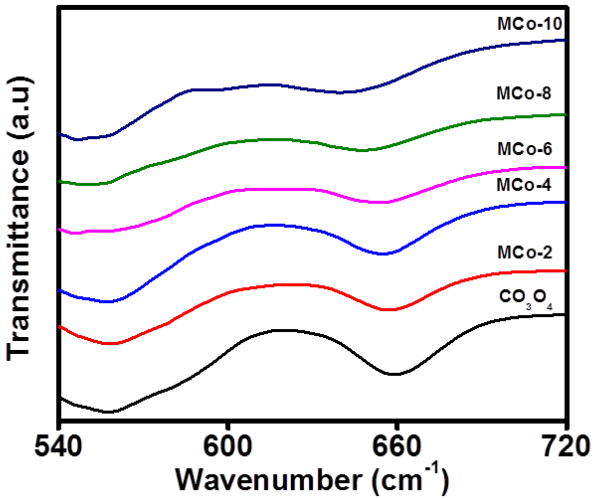

Figure 3.5: FTIR spectra of synthesized Nanocrystals.

FTIR spectra (Figure 3.5) show two strong bands which are the characteristics of crystalline Co_3O_4 due to υ(Co-O) modes at ~662 cm^{-1} and ~560 cm^{-1} which are associated with the Co^{2+} ions in the tetrahedral and Co^{3+} ions in the octahedral sites, respectively[40]. Down shift of these bands are obtained with the increasing manganese content (Table 3.2), because the atomic mass of manganese (54.93 u) is lesser than that of cobalt (58.93 u) and the ionic radii of manganese (0.645 Å) is larger than that

of cobalt (0.545 Å), which indicates that manganese is going inside the lattice which results in down shift of the two prominent vibrational bands.

Table 3.2: FTIR spectral shifts in the Metal-Oxygen bands.

Sample	*Metal-Oxygen band (cm^{-1}) (Tetrahedral site)*	*Metal-Oxygen band (cm^{-1}) (Octahedral site)*
Co_3O_4	662	560
MCo-2	657	557
MCo-4	655	556
MCo-6	652	554
MCo-8	648	553
MCo-10	643	551

Raman spectra of Co_3O_4 is having five Raman modes (A_{1g}, E_g, $3T_{2g}$) which are characteristics of single phase cubic normal spinel systems with intense A_{1g} band which corresponds to Co^{3+} in the octahedral site at ~670 cm^{-1} (41). Downshift of these bands are observed with increase in manganese content due to the atomic mass and ionic radii as explained before (Figure 3.6). It is also noticed that new Raman bands are appeared. More than five active Raman bands are features of inverse and mixed spinel systems due to the random distribution of 2+ and 3+ metal cations in the tetrahedral and octahedral sites of the spinel lattice. From these observations, it can be concluded that Co_3O_4 is formed in the normal spinel structure whereas the manganese substituted compositions $Mn_xCo_{3-x}O_4$ probably form in the inverse spinel structure.

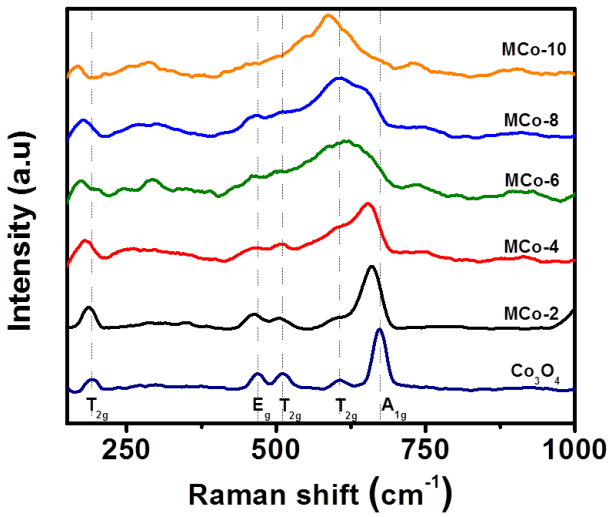

Figure 3.6: Raman spectra of synthesized samples.

3.2 ELECTROCHEMICAL STUDY

Electrochemical activity towards ORR and OER of all the catalyst were examined using RDE setup in a rotating disk electrode configuration, in which electrolyte 1 M NaOH solution was purged with oxygen gas at 1 mV/s scan rate and 1600 RPM. This low scan rate can ensure steady state behavior at the electrode surface and the rotation rate is fairly good enough to remove the bubble formation from evolved oxygen at the electrode surface.

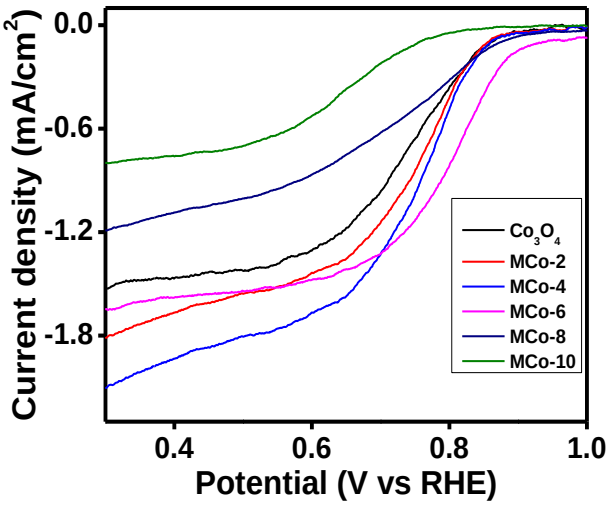

Figure 3.7: Oxygen reduction reaction (ORR) profile of all samples in O_2- saturated 1M NaOH at 1 mV/s scan rate and 1600 RPM.

Oxygen reduction polarization curves of all the samples are shown in (Figure 3.7), below 0.6 V represents the diffusion limited current and the region between 0.6 V – 0.9 V represents the kinetic diffusion control region. Out of the six LSV curves MCo-4 shows high diffusion limited current density it would be turned out to be the best candidate for ORR.

To verify the ORR pathway LSV at different rate of rotation speed were collected at 5 mV/s scan rate (Figure 3.8a), Number of electrons transferred in this ORR pathway were extracted from the Koutecky- Levich plot (Figure 3.8b), it is found that this pathway follows a four electron transfer reaction which is again proved that it can catalyse the ORR with reasonable speed.

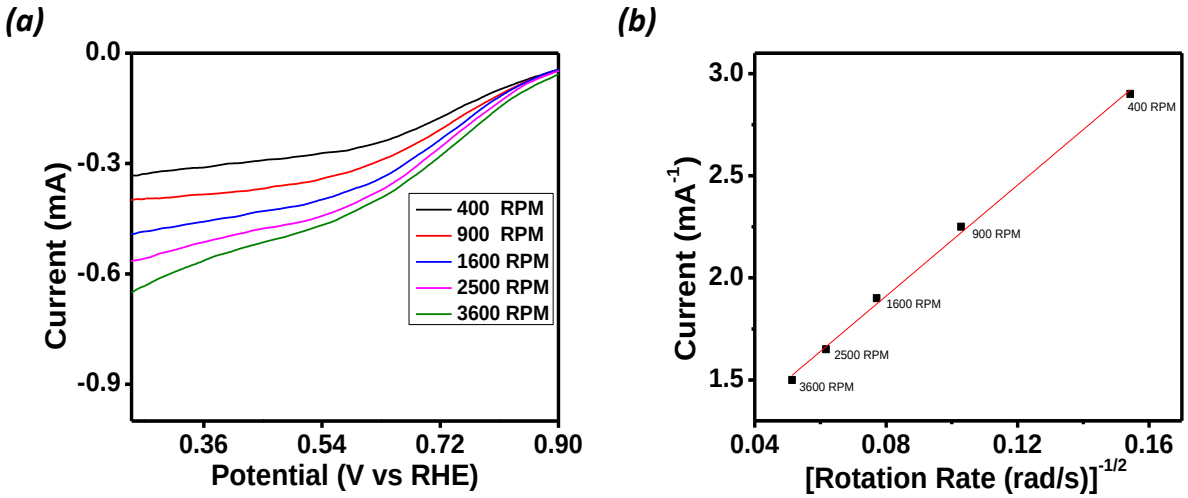

Figure 3.8: Rotating Disk Voltammogram of MCo-4 in O_2 saturated 1 M NaOH at a scan rate of 5 mV/s and different rotation rate and (b) Corresponding Koutecky – Levich (K-L) plot (I^{-1} vs $\omega^{-1/2}$).

Owing to the activity towards ORR, to use this as bifunctional catalyst in electrochemical devices such as rechargeable Metal-Air batteries activity towards oxygen evolution reaction has been investigated. All the six compounds were achieving the 10 mA/cm^2 which is the expected current density for a 10% efficient solar- fuel conversion device[42, 43]. But less overpotential is achieved by MCo-4 (figure 3.9).

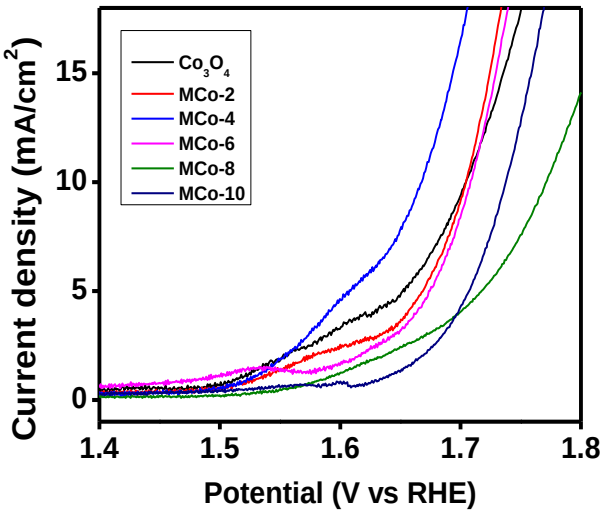

Figure 3.9: Oxygen evolution reaction (OER) profile of all samples in O_2- saturated 1M NaOH at 1 mV/s scan rate and 1600 RPM.

From both ORR and OER studies there were no particular trend can be seen with the increase in the manganese content. However in both case MCo-4 showed up higher activity. It is very difficult to predict consequence of the substitution. One can argue that it might be due to the electrochemical active surface area (ECSA), ECSA has been calculated by determining the double layer capacitance, is shown in (Table 3.3) it is clearly evident that it does not have any effect in higher activity of MCo-4. From the cyclic voltammogram of Co_3O_4 and MCo-4, the peak at 1.44 V corresponds to the oxidation peak of Co^{3+}, it is getting disappeared in the manganese containing sample. This can be concluded that manganese is getting inserted into the trivalent site, i.e., Co^{3+} is being replaced by Mn^{3+}. It is known that the presence of single electron in the e_g level of the octahedrally splitted d- orbitals of transition metal ions are the reason behind the activity[44, 45]. The single electron formation could be from high spin Mn^{3+} (t^3e^1) and low spin Co^{3+} on surface (t^5e^1), so both metal cations are catalytically active. Earlier from the lattice parameter studies it is found that with the increase in Manganese content lattice is expanding so the crystal field splitting energy will decrease, hence e^1 electronic level decreases. It can be assumed that at a particular energy level of the e^1 electron the catalytic activity is high. Beyond that increase of manganese content will decrease the activity towards ORR and OER.

Table 3.3: Electrocataltytic active surface area (ECSA) of all catalyst.

Sample	Slope (F)	Area (ECSA/cm^2)
Co_3O_4	$1.50*10^{-4}$	2.5
MCo-2	$1.43*10^{-4}$	2.3
MCo-4	$1.91*10^{-4}$	3.1
MCo-6	$2.15*10^{-4}$	3.5
MCo-8	$8.40*10^{-5}$	1.4
MCo-10	$7.75*10^{-5}$	1.3

Durability test is very important for a catalyst. Short term durability test under catalytic condition were measured by applying 10 mA/cm^2 per geometric area at 1600 RPM rotation rate, while analyzed the potential vs elapsed time and compared with the Co_3O_4 (Figure 3.10). It can clearly see that MCo-4 catalyst is stable under operating condition for 1.30 hours while Co_3O_4 loses the stability within a short time.

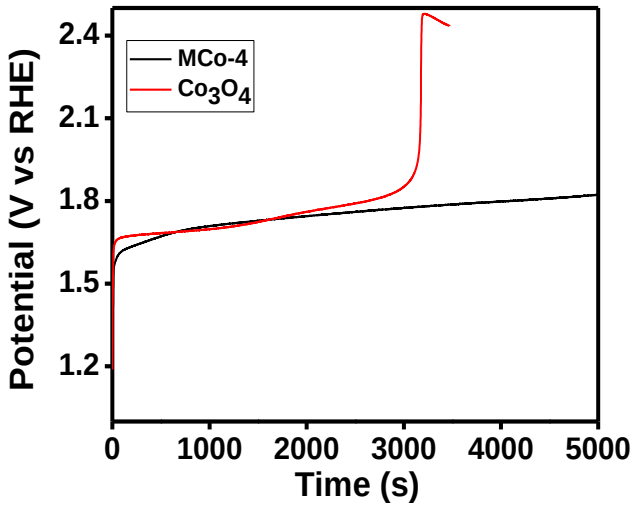

Figure 3.10: Stability test showing controlled current electrolysis of MCo-4 and Co_3O_4 at 10 mA/cm^2 per geometric area at 1600 RPM.

Oxygen formed from the OER by the catalyst were investigated in terms of Faradaic efficiency using Rotating Ring Disk Electrode. Oxidation will happen at the central disk electrode and the dissolved oxygen produced will be collected by the Pt ring electrode. (Figure 3.11) shows the both MCo-4 and Co_3O_4 ring current produced when disk electrode where subjected to a 10 mA/cm^2 current. 97% efficiency is shown by MCo-4 while Co_3O_4 shows only 87%.

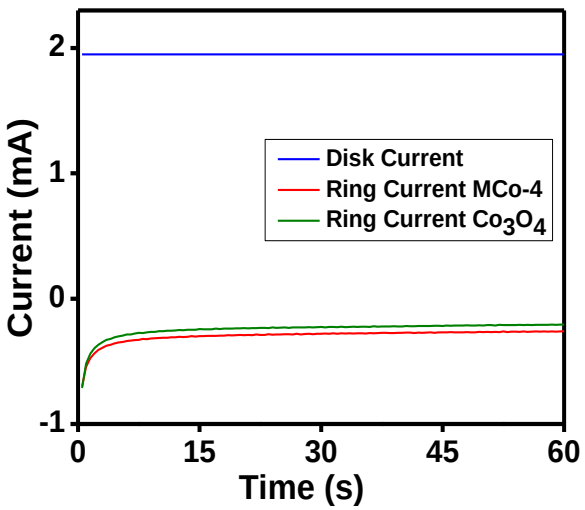

Figure 3.11: Chronoamperometric profile for the ring electrode held at 1.64 V vs RHE at 1600 RPM.

Chapter 4. CONCLUSION & FUTURE ASPECTS

Cobalt oxide nanocrystals and its metal substituted compositions $Mn_xCo_{3-x}O_4$ are successfully synthesized by using auto-combustion method and characterized using different techniques. Nanocrystals are obtained in single phase form with very low crystallite size. Metal ions simultaneously showed both lower as well as higher oxidation states, which is essential for an efficient electrocatalyst. It showed decent activity towards electrocatalytic oxygen reduction (ORR) and oxygen evolution reaction (OER) and could be used as a promising material in rechargeable Metal –Air batteries. The catalyst exhibited respectable stability and higher efficiency. Due to the lower cost and easily available material this will be used instead of existing catalyst which less is abundant and higher cost.

In future, bifunctional electrocatalyst will be used to Fabricate Rechargeable Zn – Air battery and to study its performance using different techniques. Galvanostatic polarization, charge- discharge chemistry and cycle life need to be extracted. It should be compared with the widely used existing catalyst used in Rechargeable Metal – Air battery system.

REFERENCES

1) Bruce, P. G.; Freunberger, S. A.; Hardwick, L. J.; Tarascon, J.-M. Li–O2 and Li–S Batteries with High Energy Storage. *Nat. Mater.* **2011**, *11* (2), 172–172.
2) Armstrong, R. C.; Wolfram, C.; de Jong, K. P.; Gross, R.; Lewis, N. S.; Boardman, B.; Ragauskas, A. J.; Ehrhardt-Martinez, K.; Crabtree, G.; Ramana, M. V. The Frontiers of Energy. *Nat. Energy* **2016**, *1* (1), 15020.
3) Chu, S.; Cui, Y.; Liu, N. The Path towards Sustainable Energy. *Nat. Mater.* **2016**, *16* (1), 16–22.
4) Chu, S.; Majumdar, A. Opportunities and Challenges for a Sustainable Energy Future. *Nature* **2012**, *488* (7411), 294–303.
5) Larcher, D.; Tarascon, J.-M. Towards Greener and More Sustainable Batteries for Electrical Energy Storage. *Nat. Chem.* **2014**, *7* (1), 19–29.
6) Rahman, M. A.; Wang, X.; Wen, C. High Energy Density Metal-Air Batteries: A Review. *J. Electrochem. Soc.* **2013**, *160* (10), A1759–A1771.
7) Lee, J. S.; Kim, S. T.; Cao, R.; Choi, N. S.; Liu, M.; Lee, K. T.; Cho, J. Metal-Air Batteries with High Energy Density: Li-Air versus Zn-Air. *Adv. Energy Mater.* **2011**, *1* (1), 34–50.
8) *URL:https://www.googlesciencefair.com/projects/en/2015/a20a050cd54cec76e0c708a596f9fe8997bc314157697760fabdcb0a2fef181d*
9) Li, Y.; Gong, M.; Liang, Y.; Feng, J.; Kim, J.-E.; Wang, H.; Hong, G.; Zhang, B.; Dai, H. Advanced Zinc-Air Batteries Based on High-Performance Hybrid Electrocatalysts. *Nat. Commun.* **2013**, *4* (May), 1805.
10) Zhao, Q.; Yan, Z.; Chen, C.; Chen, J. Spinels: Controlled Preparation, Oxygen Reduction/Evolution Reaction Application, and beyond. *Chem. Rev.* **2017**, *117* (15), 10121–10211.
11) Nesselberger, M.; Roefzaad, M.; Fayçal Hamou, R.; Ulrich Biedermann, P.; Schweinberger, F. F.; Kunz, S.; Schloegl, K.; Wiberg, G. K. H.; Ashton, S.; Heiz, U.; et al. The Effect of Particle Proximity on the Oxygen Reduction Rate of Size-Selected Platinum Clusters. *Nat. Mater.* **2013**, *12* (10), 919–924.
12) Wang, B. Recent Development of Non-Platinum Catalysts for Oxygen Reduction Reaction. **2005**, *152*, 1–15.

13) Greeley, J.; Stephens, I. E. L.; Bondarenko, A. S.; Johansson, T. P.; Hansen, H. A.; Jaramillo, T. F.; Rossmeisl, J.; Chorkendorff, I.; Nørskov, J. K. Alloys of Platinum and Early Transition Metals as Oxygen Reduction Electrocatalysts. *Nat. Chem.* **2009**, *1* (7), 552–556.

14) Jang, B.; Bong, S.; Woo, S.; Park, S.-K.; Ha, J.; Choi, E.; Piao, Y. Facile Synthesis of One-Dimensional Iron-Oxide/Carbon Hybrid Nanostructures as Electrocatalysts for Oxygen Reduction Reaction in Alkaline Media. *J. Nanosci. Nanotechnol.* **2014**, *14* (11), 8852–8857.

15) Kanan, M. W.; Nocera, D. G. In Situ Formation of an Water Containing Phosphate and Co 2 +. *Science (80-.).* **2008**, *321* (August), 1072–1075.

16) McCrory, C. C. L.; Jung, S.; Peters, J. C.; Jaramillo, T. F. Benchmarking Heterogeneous Electrocatalysts for the Oxygen Evolution Reaction. *J. Am. Chem. Soc.* **2013**, *135* (45), 16977–16987.

17) McDaniel, N. D.; Coughlin, F. J.; Tinker, L. L.; Bernhard, S. Cyclometalated iridium(III) Aquo Complexes: Efficient and Tunable Catalysts for the Homogeneous Oxidation of Water. *J. Am. Chem. Soc.* **2008**, *130* (1), 210–217.

18) Schulze, M.; Kunz, V.; Frischmann, P. D.; Würthner, F. A Supramolecular Ruthenium Macrocycle with High Catalytic Activity for Water Oxidation That Mechanistically Mimics Photosystem II. *Nat. Chem.* **2016**, *8* (6), 576–583.

19) Fillol, J. L.; Codolà, Z.; Garcia-Bosch, I.; Gómez, L.; Pla, J. J.; Costas, M. Efficient Water Oxidation Catalysts Based on Readily Available Iron Coordination Complexes. *Nat. Chem.* **2011**, *3* (10), 807–813.

20) Jiao, F.; Frei, H. Nanostructured Cobalt and Manganese Oxide Clusters as Efficient Water Oxidation Catalysts. *Energy Environ. Sci.* **2010**, *3* (8), 1018.

21) Wang, D.; Chen, X.; Evans, D. G.; Yang, W. Nanoscale and Oxygen Evolution Reactions †. **2013**, 5312–5315.

22) Liang, Y.; Wang, H.; Diao, P.; Chang, W.; Hong, G.; Li, Y.; Gong, M.; Xie, L.; Zhou, J.; Wang, J.; et al. Oxygen Reduction Electrocatalyst Based on Strongly Coupled Cobalt Oxide Nanocrystals and Carbon Nanotubes. *J. Am. Chem. Soc.* **2012**, *134* (38), 15849–15857.

23) Li, C.; Han, X.; Cheng, F.; Hu, Y.; Chen, C.; Chen, J. Phase and Composition Controllable Synthesis of Cobalt Manganese Spinel Nanoparticles towards Efficient Oxygen Electrocatalysis. *Nat. Commun.* **2015**, *6*, 7345.

24) Ramsundar, R. M.; Debgupta, J.; Pillai, V. K.; Joy, P. A. Co_3O_4 Nanorods—Efficient Non-Noble Metal Electrocatalyst for Oxygen Evolution at Neutral pH. *Electrocatalysis* **2015**, *6* (4), 331–340.

25) Liang, Y.; Li, Y.; Wang, H.; Zhou, J.; Wang, J.; Regier, T.; Dai, H. Co_3O_4 Nanocrystals on Graphene as a Synergistic Catalyst for Oxygen Reduction Reaction. *Nat. Mater.* **2011**, *10* (10), 780–786.

26) Chick, L. A.; Pederson, L. R.; Maupin, G. D.; Bates, J. L.; Thomas, L. E.; Exarhos, G. J. Glycine-Nitrate Combustion Synthesis of Oxide Ceramic Powders. *Mater. Lett.* **1990**, *10* (1–2), 6–12.

27) URL: http://www.veqter.co.uk/residual-stress-measurement/x-ray-diffraction

28) Elements of X-ray Diffraction, ed. by B. D. Cullity ,Addison Wesley Publishing.**1978**

29) URL:http://www.laserfocusworld.com/articles/print/volume-52/issue-10/features/spectroscopy-cvd-diamond-attenuated-total-reflection-prisms-benefit-ftir-spectroscopy.html

30) Ramer, G. and Lendl, B, *Attenuated Total Reflection Fourier Transform Infrared Spectroscopy. Encyclopedia of Analytical Chemistry. (ATR)*. **2013**

31) *URL:http://www.azom.com/article.aspx?ArticleID=10279*

32) *URL:http://www.geo.arizona.edu/xtal/geos306/geos306-12.htm*

33) C. N. Banwell, E. M. McCash, A Book: *Fundamentals of Molecular Spectroscopy,* 4th Ed. Tata McGraw Hill Publishing Co. Ltd., **2002**

34) *URL:https://chem.libretexts.org/LibreTexts/University_of_California_Davis/UCD_Chem_115/New_CV_Lab*

35) A. J. Bard and L. R. Faulkner, *Electrochemical Methods: Fundamental and Applications*, John Wiley, New York, **2001**

36) *URL:https://www.pineresearch.com/shop/knowledgebase/rotating-electrode-theory*

37) Shun Mao, Zhenhai Wen, Taizhong Huang, Yang Houa, Junhong Chen, Highperformance bi-functional electrocatalysts of 3D crumpled graphene–cobalt oxide nanohybrids for oxygen reduction and evolution reactions**,** *Energy Environ. Sci.***, 2014,** *7***,** 609

38) Stephen Treimer, Andrew Tanga , and Dennis C. Johnson, Review A Consideration of the Application of Koutecky¬-Levich Plots in the Diagnoses of

Charge-Transfer Mechanisms at Rotated Disk Electrodes**,** *Electroanalysis***, 2002,** *14***,** 165-171

39) Holzwarth, U.; Gibson, N. The Scherrer Equation versus the “Debye-Scherrer Equation.” *Nat. Nanotechnol.* **2011**, *6* (9), 534–534.

40) Sharifi, S. L.; Shakur, H. R.; Mirzaei, A.; Salmani, A.; Hosseini, M. H. Characterization of Cobalt Oxide Co3O4 Nanoparticles Prepared by Various Methods: Effect of Calcination Temperatures on Size, Dimension and Catalytic Decomposition of Hydrogen Peroxide. *Int. J. Nanosci. Nanotechnol* **2013**, *9* (1), 51–58.

41) Anantharamaiah, P. N.; Joy, P. A. Tuning of the Magnetostrictive Properties of Cobalt Ferrite by Forced Distribution of Substituted Divalent Metal Ions at Different Crystallographic Sites. *J. Appl. Phys.* **2017**, *121* (9).

42) Weber, M. F. Efficiency of Splitting Water with Semiconducting Photoelectrodes. *J. Electrochem. Soc.* **1984**, *131* (6), 1258.

43) Gorlin, Y.; Jaramillo, T. A Bifunctional Nonprecious Metal Catalyst for Oxygen Reduction and Water Oxidation. *J. Am. Chem. Soc.* **2010**, 13612–13614.

44) Suntivich, J.; Gasteiger, H. A.; Yabuuchi, N.; Nakanishi, H.; Goodenough, J. B.; Shao-Horn, Y. Design Principles for Oxygen-Reduction Activity on Perovskite Oxide Catalysts for Fuel Cells and Metal–air Batteries. *Nat. Chem.* **2011**, *3* (8), 647–647.

45) Lee, E.; Jang, J.-H.; Kwon, Y.-U. Composition Effects of Spinel $Mn_xCo_{3-x}O_4$ Nanoparticles on Their Electrocatalytic Properties in Oxygen Reduction Reaction in Alkaline Media. *J. Power Sources* **2015**, *273*, 735–741.